We are IntechOpen,
the world's leading publisher of
Open Access books
Built by scientists, for scientists

4,800
Open access books available

122,000
International authors and editors

135M
Downloads

154
Countries delivered to

Our authors are among the

TOP 1%
most cited scientists

12.2%
Contributors from top 500 universities

CLARIVATE ANALYTICS
BOOK CITATION INDEX
INDEXED

WEB OF SCIENCE™

Selection of our books indexed in the Book Citation Index
in Web of Science™ Core Collection (BKCI)

Interested in publishing with us?
Contact book.department@intechopen.com

Numbers displayed above are based on latest data collected.
For more information visit www.intechopen.com

Hidden Resources of Coordinated XPS and DFT Studies

Alexander R. Cholach

Additional information is available at the end of the chapter

Abstract

Electronic configuration of chemically bound atoms, at the surface or in the bulk of a solid, contains the traps for energy absorption provided by the valence band electron transitions; the core-level excitation of any origin is coupled with traps forming the multichannel route for energy dissipation. This chapter displays tracing over these channels by means of X-ray photoelectron spectroscopy (XPS) and density functional theory (DFT). Conformity between energy losses in the XPS spectra and electron transitions in relevant unit cells is verified by the examples of the pristine and half fluorinated graphite C_2F, and the Br_2-embedded C_2F. Perfect XPS-DFT combination can be useful for material science providing exhaustive data on state and geometry of the atoms in a sample, regardless the field of its application. The valence band is insensitive to the energy source for its excitation. It makes the behavior of energy losses in XPS spectra of the atoms to be a descriptor of bonding between these atoms in multicomponent materials. Moreover, the state of any component can be tracked through change or invariability of satellites in the relevant XPS spectra, obtained in the course of the external influence, thus revealing a wear performance of the material.

Keywords: X-ray photoelectron spectroscopy, photoelectron energy losses, valence band, electron transitions, density functional theory

1. Introduction

Fundamental studies in the field of surface science form the grounds for the sustained development of advanced technologies and new composite materials and catalysts with the desired properties [1, 2]. The methods of electron spectroscopy are unique tools of the basic research enabling characterization of the structure, composition, and properties of solids and interfaces at the atomic-molecular level.

Key properties of a sample are often exposed in their responses to a core-level excitation. The specific responses have been discovered using the tunable synchrotron irradiation and became the basis of advanced techniques [3]. The X-ray absorption fine structure (XAFS) appears near the edge of photoionization threshold (XANES) and reveals the vacant state structure, while the XAFS beyond the absorption edge (EXAFS) exhibits the local geometry [4]. The resonant inelastic X-ray scattering (RIXS) is enabled by the energy and momentum transferred by a photon near the absorption edge and exhibits the intrinsic excitations [5]. Resonant photoemission (RPES) and Auger electron spectroscopy (RAES) disclose the local electronic structure and correlations in a system, respectively [6]. The use of the electron impact instead of the X-ray, as a source of the core-level excitation, has discovered the similar effects of the conjugate electron excitation (CEE) [7–11]. The CEE shows itself as a set of satellites in disappearance potential spectra (DAPS), which answers to valence band (VB) structures of near-surface atoms, including the adsorbed species, and plasmon excitations. Experimental evidence for the CEE phenomenon is based on DAPS spectra, obtained from various adsorbed layers and on its mechanism represented by the combination of ordinary electron transitions. For example, plasmon oscillations are often observed by means of X-ray photoelectron (XPS) and Auger electron spectroscopies (AES) [12, 13]. Ionization of the VB, of the substrate and adsorbed species, is a basis of ultraviolet photoelectron spectroscopy (UPS) [14]. Similar satellite structures, above different thresholds, in DAPS spectra confirm that the core electrons are identical with regard to CEE transitions [7, 8]. CEE phenomena represent, in whole, the multichannel route for energy dissipation within the DAPS probing depth of 2–3 monolayer (ML), which does not undermine the general concepts in the field of electron scattering.

Novel as well as advanced technologies strongly require the next generation materials in the fields of tribology [15–17], hardness [18, 19], corrosion and wear performance of the material [20], and many others [21–23]. The progress of material science in these fields is resulted, in large measure, from the fundamental studies by means of modern techniques, including the XPS as well [16, 17, 21–23]. The X-ray photoelectron spectroscopy is a powerful analytical tool; however, this method is limited by the content and charge state of the atoms, while it cannot disclose the chemical behavior and structural features of the atoms in a sample, which are urgently needed in case of the multicomponent substrate. These properties and many others are direct products of the DFT. In turn, the DFT runs give greatly different results depending on starting conditions and the operational parameters, which have to be found indirectly. A reliable intersection between the XPS and DFT outputs would help to employ the hidden resources of both techniques.

The CEE phenomenon is a true multi-channel route of energy dissipation through the VB. The identity of electronic nature of the surface and bulk atoms allows one to suggest the similarity of inelastic electron scattering mechanisms on the surface and in the bulk of a solid. Then, the CEE should also occur, under the X-ray core-level excitation, and manifest itself in the XPS spectra as energy losses. The plasmons in AES and XPS spectra correspond indeed to the collective CEE phenomena. Highest occupied molecular orbital-lowest unoccupied molecular orbital (HOMO-LUMO) transitions, which are often used for assignment the XPS, RPES and XANES spectra [24, 25], are also clear CEE manifestations. The electron energy dissipation, accompanying the core-level excitation, is the general trend of any electronic configuration.

Auger transitions are particular cases of the event resulted from filling the core hole. CEE is another route of relaxation consisting in redistribution of the photoelectron energy through the accessible valence bands.

A close attention is paid to the graphite materials as essential parts of the advanced technical devices [26]. Fluorinated graphite serves as an intermediate of the graphene synthesis, while embedded with the alkali or halogen, exhibits high chemical stability, improves the anode activity in a fuel cell, becomes the nano-reactor or the storage nano-container of volatile compounds, and so on [27–29]. We have considered highly orientated pyrolytic graphite (HOPG), half-fluorinated HOPG (C_2F), and that with the embedded Br_2 (C_2F *0.15Br) as touchstones of the following concept [30, 31]. First, inelastic electron scattering, in near-surface layer and in the bulk of a solid, follows the same regularities. Second, the X-ray core-level excitation is accompanied by the VB transitions revealing themselves as the photoelectron energy losses. Third, linking of the XPS and DFT methods via conformity between XPS spectral structures and theoretical CEE transitions justifies the other DFT products related to local geometry, chemical bonding, and states of the atoms in a sample.

2. Experimental

Inelastic electron scattering has been monitored by the elastic scattering, using the DAPS. Disappearance potential spectroscopy is based on the threshold core-level excitation by an electron beam of the time-based energy E_p [32]. Whenever the incident potential exceeds the core-level energy, a part of electrons disappears from the elastic current I and provides a dip in the dependence of $dI(E_p)/dE_p$ on E_p. The event occurs if E_p is equal to difference between the core and vacant state energy. The spectrum shape is determined by the self-convolution of vacant density of states (DOS), as the destination of interacting electrons. The adsorption of test gases over the Auger-clean Pt(100)-(1 × 1) single crystal was performed at 300 K [33]; exposures are given in Langmuir (1 L = 10^{-6} Torr s). The Fermi level (E_F) in DAPS spectra corresponds to E_p = 314.8 eV, which is close to the reference $Pt4d_{5/2}$ core-level energy [34]. Other experimental details and the spectrum processing can be found elsewhere [7–11].

The XPS studies were performed on a Phoibos 150 SPECS spectrometer (Germany) using monochromatized Al K_α radiation (1486.7 eV). The backgrounds of external and surface energy losses in XPS spectra have been subtracted [35]. Other experimental details, the low-temperature synthesis technique, and characterization of HOPG, pristine and fluorinated C_2F can be found elsewhere [36, 37]. The Br_2 embedding into C_2F was performed as in Ref. [38] and resulted in the ~$C_2FBr_{0.15}$ stoichiometry.

3. Theoretical

Geometric parameters and DOS of the unit cells were calculated by the density functional theory using the Quantum ESPRESSO Software [39] and the nonlocal exchange-correlation functional

in the Perdew-Burke-Ernzerhof parameterization [40]. The interactions between ionic cores and electrons were described by the projected augmented wave (PAW) method [41] with the kinetic energy cutoff E_{cut} = 40 Ry (320 Ry for the charge-density cutoff) for a plane-wave basis set. The Gaussian spreading for the Brillouin-zone integration was 0.02 Ry; the Marzari-Vanderbilt cold smearing was used [42], and the van der Waals (vdW) corrections were included [43].

The Pt DOS was calculated using the Perdew-Burke-Ernzerhof functional [44] and the PAW with the optimized lattice constant 3.99 Å. The kinetic energy cutoff E_{cut} = 40 Ry and a 12 × 12 × 12 grid of Monkhorst-Pack k-points were applied.

HOPG was modeled with a bilayer C_{24} unit cell of the Bernal and Hexagonal (*hex*) structure (**Figure 1**) and optimized lattice parameters (a = 2.46 Å × 3, b = 2.46 Å × 2) [45].

Half-fluorinated graphite, pristine and imbedded with the Br_2 molecule, was modeled with a bilayer $C_{24}F_{12}$ and $C_{24}F_{12}Br_2$ unit cell, respectively, with the optimized lattice parameters a = 2.49 Å × 3, b = 2.48 Å × 2 for the *hex* structure and a = 2.50 Å × 3, b = 2.48 Å × 2 for the Bernal structure. The F was attached to C atoms all outside and half inside and half outside a cell (**Figure 1**) with 40 Bohr space between slabs to prevent the interactions. In latter case, the entry interlayer distance d_{layer} in a $C_{24}F_{12}Br_2$ unit cell was taken larger by 2 Å than optimized d_{layer} in a $C_{24}F_{12}$ unit cell (in order to avoid unrealistic Br_2F formation or F $\leftrightarrow$ Br_2 replacement under relaxation of the system), in line with experimental measurements [46]. All atoms were allowed to move free under an optimization of the unit cells. The Brillouin-zone integration was performed on a 20 × 20 × 1 grid of Monkhorst-Pack k-points [47]. The accuracy was verified by testing the energy convergence. The default numbers of bands were used for free bromine particles.
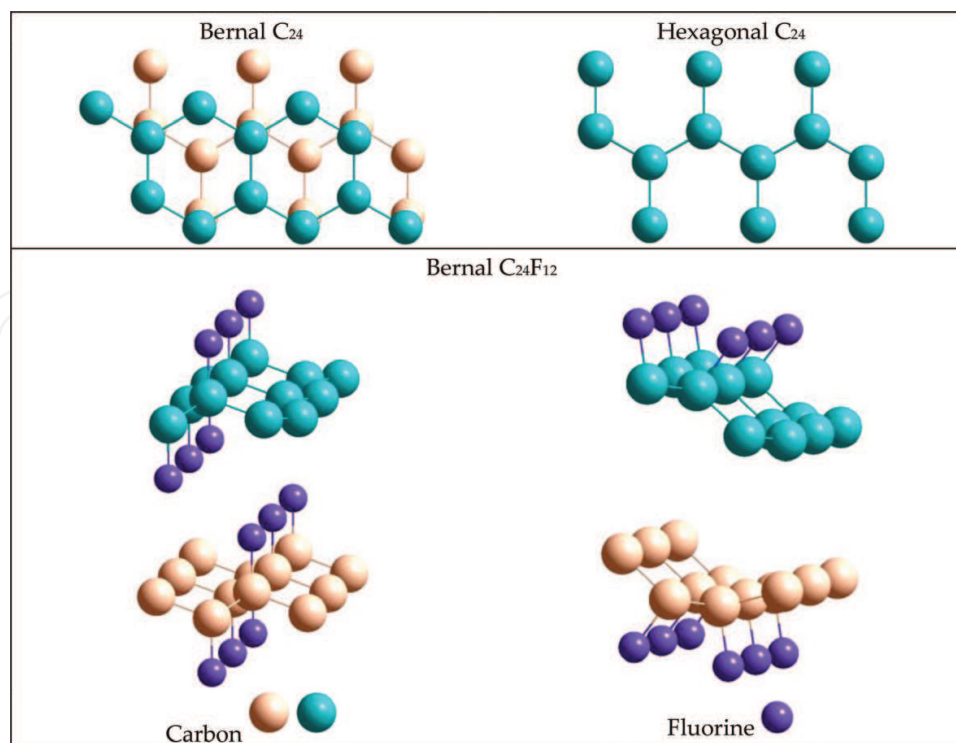

Figure 1. Unit cells C_{24} with the Bernal and *hex* structure (top panel) and unit cell $C_{24}F_{12}$ Bernal with arrangement of the F atoms half inside and half outside and all outside a cell. Adapted from [30].

4. Inelastic electron scattering in near-surface layer

DAPS theory directs core and primary electrons to nearest vacant states above E_F [32]. The larger is the vacant DOS, the larger is the spectral dip, and the lack of free DOS gives no signal. The DAPS technique discovers all channels of the elastic electron consumption, which are specifically related to CEE phenomena and consisted of shake-up and shake-off VB transitions coupled with the threshold core-level excitation of an atom. These channels are electron transitions from the ground σ_{VB} to vacant DOS σ_{Vac} and the vacuum level, whose probability $W(E)$ is in proportion to the corresponding convolution and σ_{VB}, respectively, on the absolute energy relative to E_F with a matrix element $f(E, \sigma)$:

$$
\begin{aligned}
W_{up}(E) &= \int_0^E f(E, \sigma)\, \sigma_{VB}(-E)\, \sigma_{Vac}(E - \varepsilon)\, d\varepsilon \\
W_{off}(E) &= f(E, \sigma)\, \sigma_{VB}(\varphi - E)
\end{aligned}
\tag{1}
$$

The shake-off CEE moves σ_{VB} to free DOS at the vacuum level. According to the Rutherford relation $ds/d\Omega \sim \sin^4(\Theta/2)$, the cross-section for the nonrelativistic scattering is efficient for small angles Θ [48, 49]. The probability $W(E)_{off}$ in Eq. (1) therefore includes one-dimensional (1D) free DOS. According to Van Hove singularities, the 1D DOS is equal to 0, infinity, and $1/\sqrt{E - E_F - \varphi_{Pt}}$ at the energies below, at, and above the vacuum level, respectively [50], as shown in **Figure 2(a)** (where $\varphi_{Pt} = 5.6$ eV is the work function of Pt(100) [51]). This provides the resonant CEE behavior and multiple tracing over the adsorbed species (including hydrogen atoms and reaction intermediates) around different thresholds [8–11]. The shake-off satellite of adsorbed particle is an intense peak of the 1–2 eV base-width and coverage-proportional intensity, which is located at its ionization potential above the Pt threshold. The DAPS spectra in **Figure 2** particularly exhibit the σ state of the H_{ad} atom and 1π, 5σ, and 4σ states of the CO_{ad} molecule, which fit published UPS data in **Table 1** [52–55]. Similar accordance between the DAPS and UPS measurements has been found for the adsorbed O, N, NO, and NH species [7].

The Pt shake-off spectrum in **Figure 2(b, c)** was constructed on the basis of DFT data as follows. The VB was inverted (because the larger σ_{VB} the larger $W_{off}(E)$ in Eq. (1), and the larger the spectral dip); differentiated, and shifted to the higher energy by φ_{Pt}. Adsorbed layer makes significant contribution into the DAPS spectrum due to superior surface sensitivity of this technique, whose probing depth 2–3 ML is determined by half the electron mean free path in a solid. The Pt shake-up spectrum in **Figure 2(b)** corresponds to convolution of the occupied and vacant d states by Eq. (1). The calculated Pt shake-up and shake-off spectra in **Figure 2** are close to each other due to strongly localized vacant states at E_F and the 1D DOS at the vacuum level, respectively, and because of domination of the equal d_{zx}, d_{zy}, and d_{xy} states in total DOS [30]. An agreement between experimental and simulated spectral fragments in **Figure 2** implies regular involvement of the Pt DOS into CEE events, as well as similar matrix elements $f(E, \sigma)$ for different partial densities of states (pDOS) in Eq. (1) and no symmetry ban for CEE transitions.

Figure 2(b) demonstrates tracing over the adsorbed hydrogen atoms, which is beyond AES and XPS facilities. It is important to note that none of the satellites in the DAPS spectra was assigned to the interatomic CEE transition (from the VB of the adsorbed species to free state of
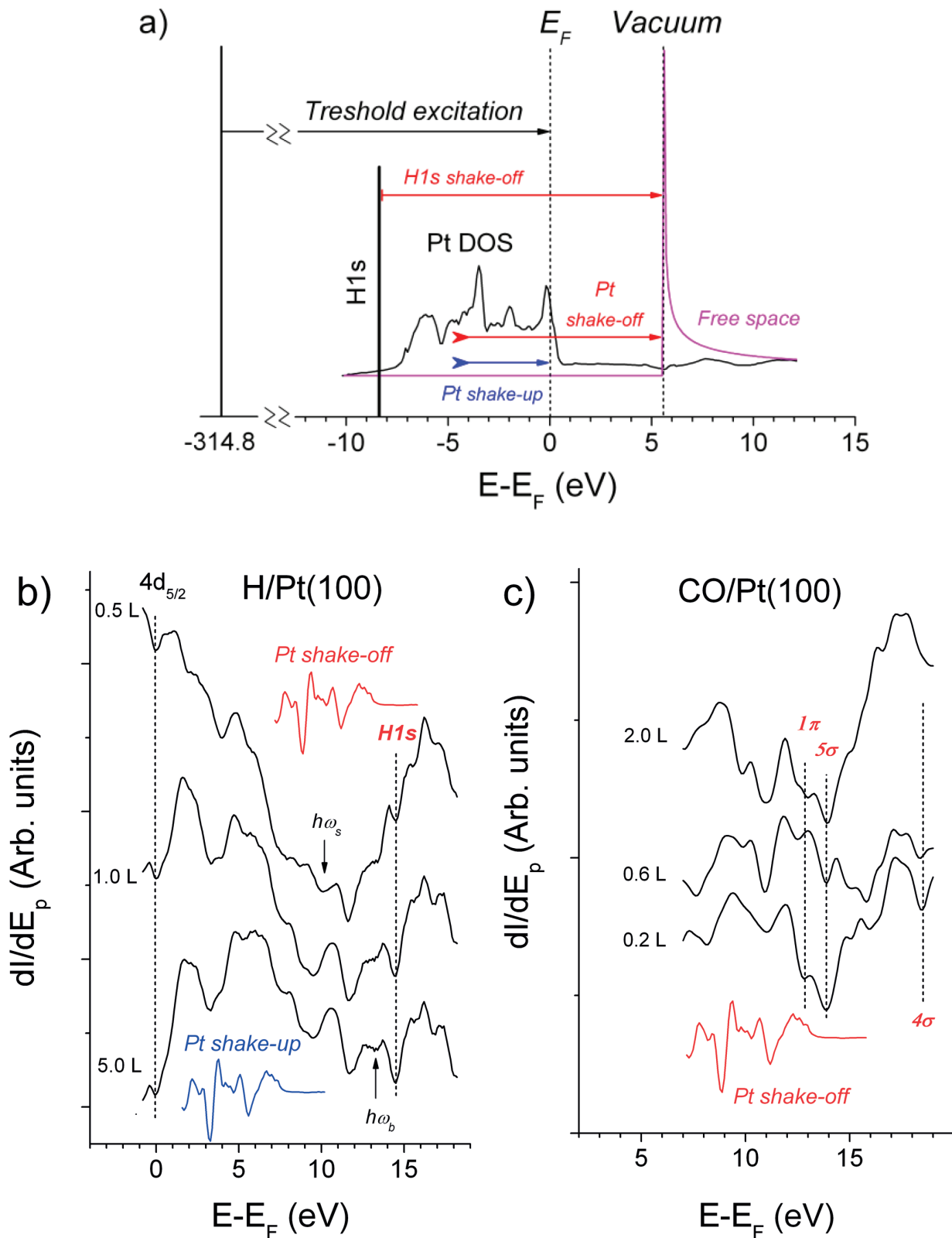
Figure 2. (a) General scheme of the CEE transitions by an example of H/Pt(100) system exposed to primary electron beam with energy above the $Pt4d_{5/2}$ threshold. (b) Difference DAPS spectra obtained after exposure of Pt(100) surface to H_2; colored curves indicate the Pt shake-up and shake-off satellites expected from (a). (c) DAPS spectra obtained after exposure of Pt(100) surface to CO; red curve shows the Pt shake-off satellites expected from (a). Adapted from [8].

Sample	O	H	CO			Source
Satellite	*O2p*	*H1s*	*1π*	*5σ*	*4σ*	
Gas	13.6	13.6	14.0	16.5	19.7	[34]
H/Pt(100)-(1 × 1)		13.7				**Figure 2a**
H/Pt(111)		12.8				[57]
CO/Pt(100)-(1 × 1)			12.7	13.7	18.3	**Figure 2c**
CO/Pt(111)			14.2	15.1	17.5	[53–55]
CO/Pt(100)-*hex*			13.4–15.8		16.4–18.0	[53]
O/Pt(100)-(1 × 1)	14.0					[10]
O/Pt(100)	12.7					[53]
O/Pt(111)	14.2					[12]
O/Pt(111)	12.1					[54, 57]

Table 1. Peak minima in the DAPS spectra as compared with the reference UPS data (eV).

the metal atom) [8, 10]. Furthermore, the surface plasmon disappears while the bulk plasmon decreases on coverage in **Figure 2(b)** because of screening by the adsorbed layer, in contrast to behavior of the VB CEE satellites [9]; multiple plasmons were also detected at relevant energy points [7]. Conformity between the calculated and experimental data in **Figure 2** indicates that the vacancies, at E_F and at the vacuum level as well, are appropriate spots of destination of the electrons under their CEE transitions. Present consideration confirms the generality of CEE phenomena under the inelastic electron scattering in the adsorbed system. The CEE control is an additional tool of electron analyzer for fingerprinting the adsorbed layer and an alternative to the RPES, which requires a tunable synchrotron irradiation and special instrumentation [6]. Besides that, the DAPS provides the vacant state structure and geometrical parameters similar to XANES and EXAFS, respectively [56].

CEE satellites of the adsorbed species accompany the threshold core-level excitation of that neighboring atom, which is bound to the above species, while core-level energies are easily distinguishable. Therefore, the CEE control empowers localization of the adsorbed species over multicomponent surface. CEE regularities in the near-surface layer can be summarized as follows:

- Shake-up transitions correspond to convolution of the occupied and unoccupied pDOS of the same atom and likely have no symmetry ban.

- Shake-off transitions are available for the substrate atom and adsorbed species as well, where the former is the energy source; the 1D DOS at the vacuum level is a common VB destination. There is no symmetry prohibition, and the satellite structure is a VB mirror-image with respect to E_F, shifted to higher energy by the work function.

- Plasmon oscillations give evidence for the collective CEE phenomenon.

5. Conjugate electron excitations in the bulk of a solid

The CEE phenomena occur with high probability in the near-surface layer of 2–3 ML [7–10]. Electronic affinity between surface and bulk atoms assumes similar channels of the inelastic electron scattering under the core-level excitation, no matter by primary electrons or X-ray irradiation. The photoelectron can partially lose its energy for the CEE transition and exhibits the VB peculiarities in fine XPS spectral structure. By analogy with the above findings, CEE phenomena in the bulk of a multicomponent material, under the nonresonant X-ray core-level excitation, can be characterized as follows:

- Shake-off transitions are available, where pDOSs must be considered due to probable difference in their matrix elements. The same ground state (VB), the common destination (the vacuum level), and enough energy excess of any of the photoelectrons should result in analogous energy losses in the XPS spectra of different components of a sample.

- Shake-up transitions are available, in which the convolution should include pDOSs of the same atom. The VB of chemically bound atoms has no preference for a photoelectron to detach its energy for the CEE transition, and so similar energy losses are also expected in the XPS spectra of different components of a sample.

This chapter focuses on the DAPS omitting the allied threshold excitation techniques of the Auger electron and soft X-ray appearance potential spectroscopies, which follow the core hole decay and are complicated, at least, by the electron-core hole interaction [32]. In contrast, the DAPS fixes origination of the core hole, when the electron–hole interaction is not yet occurred or minimal. The same is true for energy losses in the XPS spectra because the photon absorption and the CEE energy dissipation can proceed at once or shortly, thus eliminating or minimizing the electron-core hole interaction, respectively. It is worth noting that CEE events are enabled by belonging of former core and valence band electrons to the same configuration and can be hardly detectable by electron energy loss spectroscopy, while the AES spectra are usually complicated by the background.

5.1. HOPG and half-fluorinated graphite C_2F

DFT runs have revealed that density of states in **Figure 3(a)**, obtained for the C_{24} unit cells with the Bernal and *hex* structure, are similar and close to the DOS of graphite/graphene [58]. The optimized C-C bond length d_{C-C} = 1.42 Å and the interlayer distance d_{layer} = 3.34 Å in *hex* C_{24} also fit to those of the graphite. The Bernal C_{24} structure reveals the larger formation energy and smaller d_{layer} by ~0.3 Å due to stronger interaction between the layers as compared to *hex* C_{24} structure.

Conventional satellites at higher energy sides of the XPS spectra correspond indeed to the photoelectron energy consumption. The CEE approach enables complete description of the HOPG XPS C1s spectrum in **Figure 3(b)** by the combination of shake-up and shake-off CEE transitions.

The satellite ~5.5 eV in **Figure 3(b)** is assigned to a π plasmon responsible for the $\pi \rightarrow \pi^*$ transition [59], although the standard plasmon is related to the collective oscillations of free
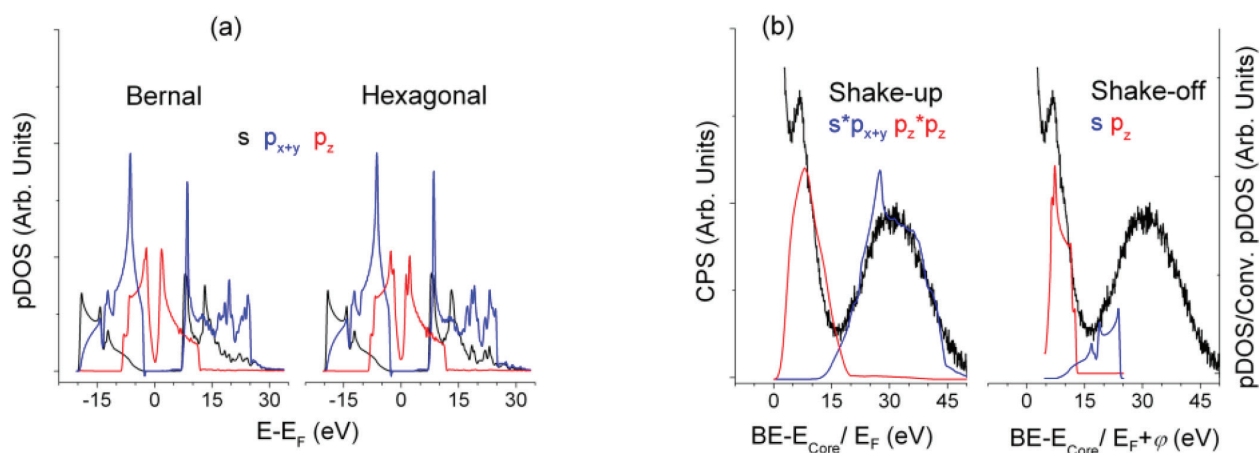
Figure 3. (a) Partial DOS for the unit cells C_{24} with the Bernal and *hex* structure ($p_x = p_y$); (b) shake-up and shake-off CEE transitions in the unit cell *hex* C_{24} as compared to energy losses above the core-level energy (284.6 eV) in the XPS C1s spectrum of HOPG. Adapted from [31].

electrons missing in HOPG [60].This satellite originates rather from the shake-off than from the shake-up p_z transition (**Figure 3(b)**).

There is expected similarity between higher energy tails of the $^{(F)}$C1s (C is bound to F) and F1s XPS spectrum in **Figure 4**, which emphasizes the indifference of the VB with respect to energy source for the CEE transition. Fine XPS spectral structures above 10 eV conform well to shake-up (**Figure 4(a)**) and shake-off (**Figure 4(b)**) CEE transitions calculated by Eq. (1). The matrix elements $f(E, \sigma)$ in Eq. (1) were accepted unity for a $W(E)$ basis set, while the Y-scale factors in **Figure 4** (a, b) evaluate $f(E, \sigma)$ and the contribution of a particular CEE transition, in total theoretical energy consumption, to fit the experimental photoelectron energy losses.

The π plasmon at ~5.4 eV in **Figure 4(a, b)** is assigned to the conjugated π bonds in a chain of C atoms [37]. This feature fits the shake-up Cp_z transition and accompanies the C1s spectrum, since the π bond is localized exclusively at the Csp^2 atom, not bound to F. Similar feature is exhibited in the C K- and not exhibited in F K-edge XANES spectra of C_2F [29], and the π plasmon is certainly not observed the XPS C1s spectrum under the lack of π-bonds [61]. Discovery of a similar satellite in the F1s spectrum is rather confusing because F atoms have nothing to do with the π bond between C atoms), but it is quite in line with the CEE model.

The base line shift relative to C1s = 285.1 eV in **Figure 4** (C is not bound to F) saves accordance with the DFT data and enables to make a contribution to the energy loss ~5.4 eV to the other shake-off transitions ($^{(F)}Cp_y$, Fp_y, Fp_z). The formation energy of the Bernal unit cell $C_{24}F_{12}$ is by 0.008 eV higher than that of the *hex* $C_{24}F_{12}$ cell, while pDOSs of both structures are very similar. A sizable DOS at E_F accepts plasmon oscillations that can give the energy loss at 9.1 or 12.9 eV for 1 or 2 free electrons per a C_2F fragment, respectively [30].

5.2. Br$_2$-embedded C$_2$F

XPS spectra obtained after the Br$_2$ intercalation into C_2F matrix reveal stoichiometry $C_2FBr_{0.15}$ and the lack of new features compared to XPS spectra of the pristine C_2F (**Figure 4**); C1s and F1s spectra are in agreement with the same CEE transitions as before the Br$_2$ embedding. DFT
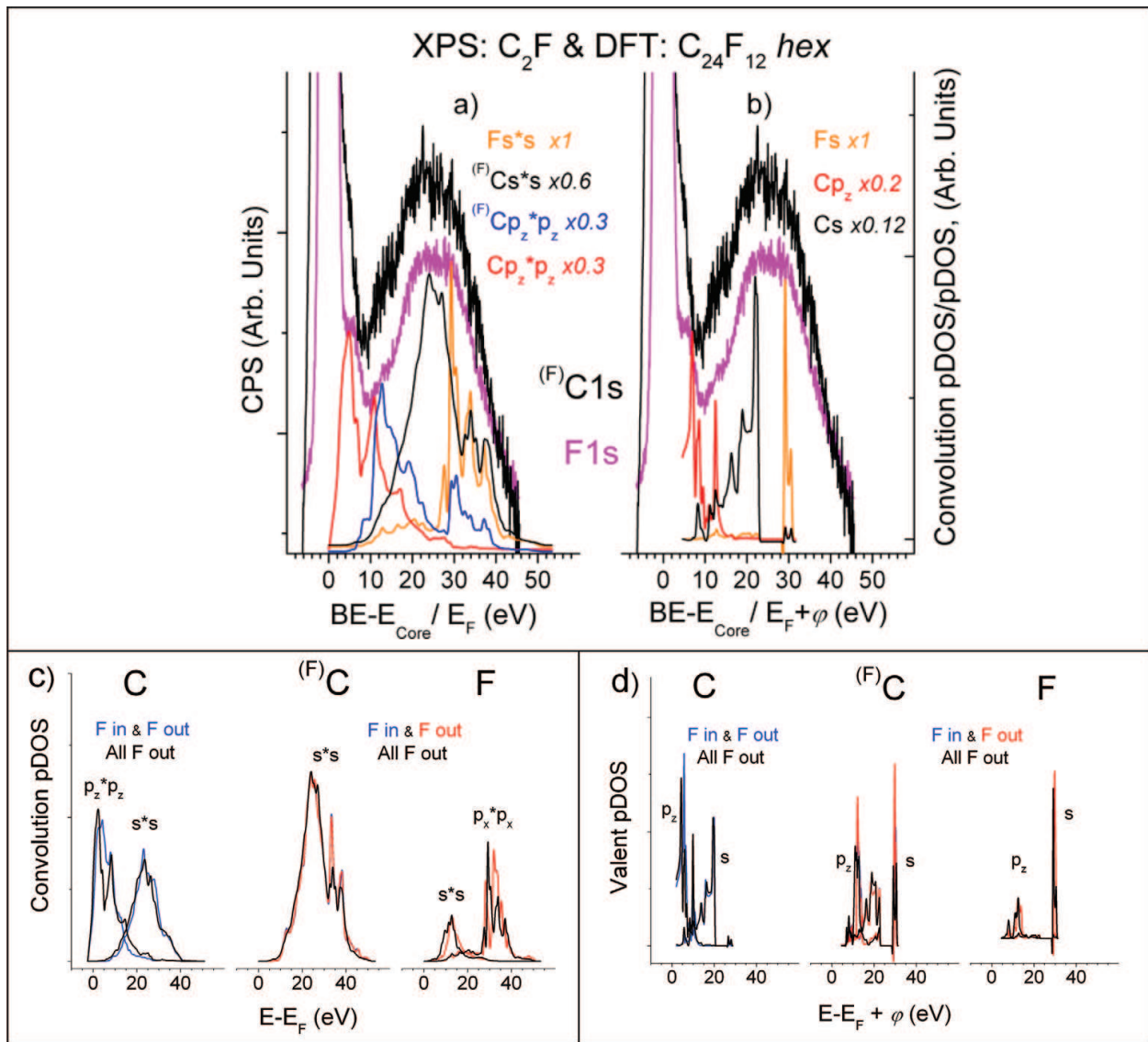
Figure 4. XPS C1s and F1s spectrum of C_2F (relative to E_{Core} = 287.6 eV and 687.4 eV, respectively; the background of external and surface energy losses are subtracted [35]) and shake-up (a) and shake-off (b) transitions of $^{(F)}C$ and F atoms forming the C-F bond in the unit cell *hex* $C_{24}F_{12}$ (all F are outside). (c) Shake-up and (d) shake-off CEE transitions for different arrangements of the F atoms (**Figure 1**). Adapted from [31].

studies were performed for the Bernal and *hex* $C_{24}F_{12}Br_2$ unit cells #1–9 in **Table 2** at the entry angles α_0 = 0 and 90° between the Br-Br axis and C planes and different arrangements of the F atoms (**Figure 1**).

DFT calculations have revealed that the Br_2 embedding enlarges the interlayer distance, but insignificantly affects the pDOS of the C, $^{(F)}C$ and F [30]. The latter conforms to chemical inertness of the pristine C_2F cell and to low Br content in the product $C_2FBr_{0.15}$ [62]. Invariant pDOS of the C and F atoms and slight change in the C1s and F1s XPS spectra, after the Br_2 embedding into $C_{24}F_{12}$ framework, restrain the correlation between XPS and DFT outputs. The novelties of XPS and DFT data, which are resulted from the Br_2 embedding, concern the bromine only and are considered in more detail.

Species/unit cell	d_{BrBr} (Å)	α (optimized)	$\Delta_{s\text{-}p}$ (eV)	Br state
Free Br_2^0	2.29	—	12.806	Molecular
Free Br_2^{-1}	2.89	—	12.061	Molecular
Free Br_1^0	—	—	12.285	Atomic
Free Br_1^{-1}	—	—	11.730	Atomic
All F out a cell (**Figure 1**)				
#1 *hex* ($\alpha_0 = 0°$)	3.24	0.0°	11.66	Atomic
#2 *hex* ($\alpha_0 = 90°$)	2.45	51.5°	12.06	Molecular
#3 Bernal ($\alpha_0 = 0°$)	2.375	6.2°	12.32	Molecular
#4 Bernal ($\alpha_0 = 90°$)	3.18	0.1°	12.68	Atomic
#5 Bernal ($\alpha_0 = 52°$)	3.34	0.8°	12.61	Atomic
Half F in & half F out a cell (**Figure 1**)				
#6 *hex* ($\alpha_0 = 90°$)	2.44 (nearest)	17.4°	12.09	Chain type
	2.73 (next nearest)			
#7 *hex* ($\alpha_0 = 0°$)	2.30 (nearest)	12.9°	12.82	Molecular
	4.96 (next nearest)			
#8 Bernal ($\alpha_0 = 90°$)	2.44 (nearest)	17.2°	12.15	Chain type
	2.73 (next nearest)			
#9 Bernal ($\alpha_0 = 0°$)	2.29 (nearest)	18.7°	12.97	Molecular
	4.96 (next nearest)			

Table 2. Br-Br distance d_{BrBr}, angle α between the Br-Br axis and C-planes, and difference $\Delta_{s\text{-}p}$ between the weighted average Br *s*- and *p*- DOS in free species and unit cells $C_{24}F_{12}Br_2$.

The difference F1s spectrum in **Figure 5** exhibits a distinct structure, which conforms to shake-up transitions of the pDOS responsible for C-F bonding and which is interpreted as the C-F bond strengthening [30]. It can be the case since the Br_2 embedding weakens the interactions between carbon layers, which should be accompanied with the enrichment of the occupied DOS of C and F. Arrangement of the F atoms in a cell makes no matter for the conclusion.

DFT studies have found a set of cells $C_{24}F_{12}Br_2$ with the optimized parameters and different local geometry and the state (atomic, molecular, and chain type) of the embedded Br_2 (**Table 2**). Each of nine local structures is appropriate; no preference can be given to a particular cell from the conventional DFT study.Each of these unit cells is characterized by the specific Br pDOS structure [30]. DFT examinations of separate bromine species revealed a strong difference $\Delta_{s\text{-}p}$ = 0.2–1.3 eV between the weighted average energy $<E_{s,p}>$ of the Br *s*- and *p*- DOS, far beyond the accuracy of DFT runs ~0.01 eV (**Table 2**). The parameter $<E_{s,p}>$ was determined as E, $\sum \sigma_i E_i / \sum \sigma_i$ and middle of $\int \sigma_i d E_i$ for the Br atom with single, several localized, and diffused *s*- and *p*- DOS, respectively. In the same way, as the binding energy determines the oxidation rate in extensive XPS practice; the parameter $\Delta_{s\text{-}p}$ was taken as a descriptor of the Br state [30].
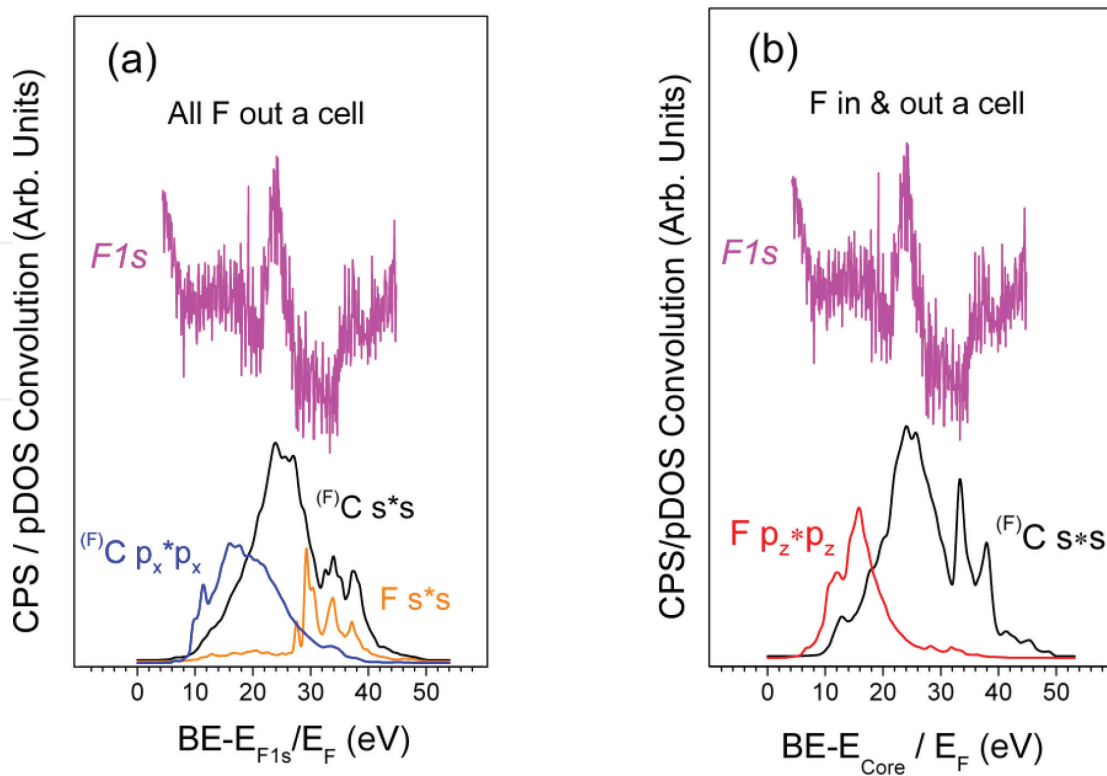
Figure 5. Difference XPS F1s spectrum (F1s C_2F was subtracted from F1s $C_2FBr_{0.15}$) as compared to shake-up VB transitions for the unit cells $C_{24}F_{12}Br_2$ (a) #2 and (b) #6 in **Table 2** with different layout of the F atoms (**Figure 1**).

For the unit cells with all F atoms outside, the minimal deviations Δ_{s-p} of 0.02, 0, and 0.04 eV make preferable the cells #1, #2, and #3, respectively (**Table 2**). Moreover, in case of the large d_{BrBr} (the Br-Br bond is lost), the difference Δ_{s-p} in a cell should be close to that of free Br_1^0. Otherwise (the Br-Br bond retains), the difference Δ_{s-p} should be close to that of the Br_2^0 species. In this case, d_{BrBr} for cell #1 (3.24 Å) and cell #2 (2.45 Å) is adequate to the lack of the Br-Br bond in Br_1^{-1} and to the eigenvalue of Br_2^0 (2.29 Å), respectively. On the contrary, the cell #3 should be ruled out, because its d_{BrBr} = 2.37 Å indicates retaining the Br-Br bond while the Br_1^0 specimen, with nearest Δ_{s-p}, has no bond. Finally, the cell #2 wins the cell #1 in the formation energy (**Table 1**). Besides, the reaction $C_{24}F_{12} + Br_2 \rightarrow C_{24}F_{12}Br_2$ is endothermic for cell #1, in contrast to other cells [30].

The bromine p_z- and s- shake-off transition conforms to the nonresolved 5–12 eV fragment and ~20 eV shoulder of the Br3d spectrum in **Figure 6(a)**, respectively. The higher energy parts of the XPS Br3d, F1s and C1s spectra are similar [30], but they do not correlate with any of the Br CEE transitions. This indicates such a bonding between the Br_2 molecule and the C_2F frame that provides the Br3d photoelectron energy losses via CEE transitions of pDOS of the C and F atoms.

DFT calculations for the unit cells $C_{24}F_{12}Br_2$, with the F atoms half inside and half outside a cell, have revealed two stable Br_2 states. The first state, in cells #7 and #9, corresponds to Br_2 pairs (**Table 2**), which are separated from each other in the adjacent cells and exhibit the same Br-Br distance d_{BrBr} ~2.29 Å as in a free Br_2 molecule. The second state (cells #6 and #8) corresponds to Br arrangement as the chain, in which d_{BrBr} ~2.44 Å within a unit cell is larger than in a free
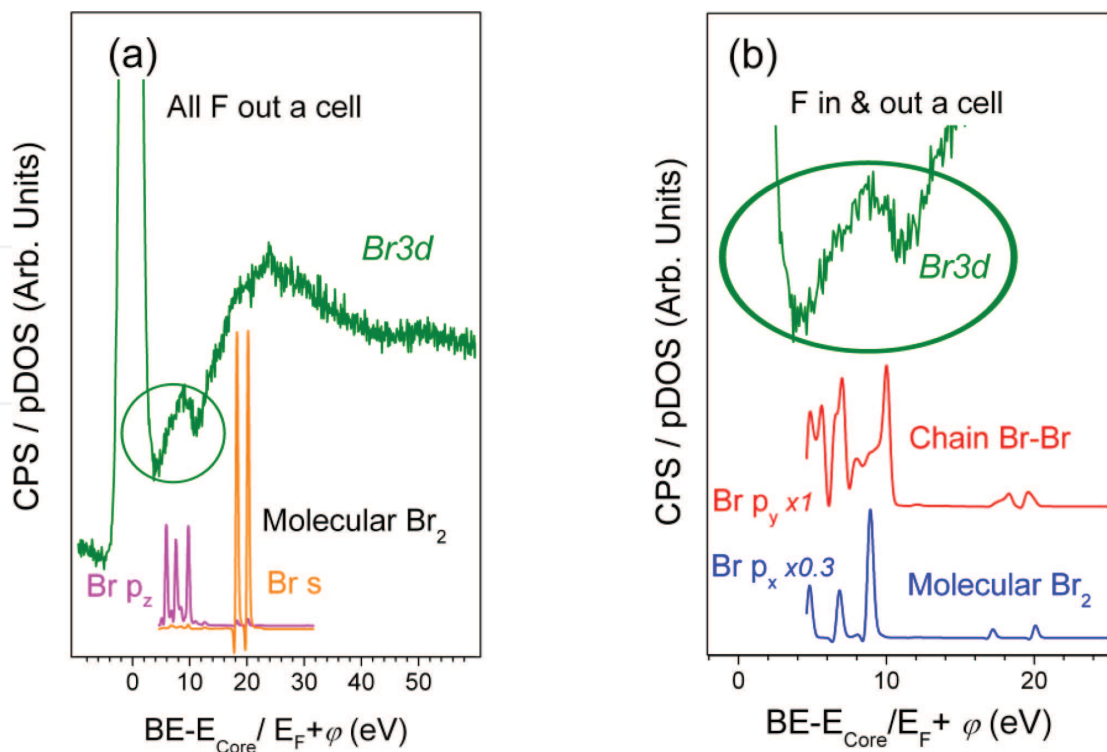
Figure 6. Br3d XPS spectrum of $C_2FBr_{0.15}$ as compared to relevant shake-off VB transitions of the Br atom in unit cells with different F layout (a) #2 (*hex*), and (b) #8 and #9 (Bernal).

Br_2, while nearest distance between the Br atoms of the adjacent cells 2.73 Å is smaller than the nearest intermolecular distance in a solid Br ~3.37 Å [63] and still enough for the vdW interaction [45]. There is no visible difference in the Br pDOS of cell #6 and #8 (chain type Br), while there is a few difference between the Br p_x and p_y states for cell #7 and #9 (molecular Br_2). Finally, the weighted average Δ_{s-p} values are line with the molecular Br state for cells #7 and #9; the state close to Br_2^{-1} for cell #6; and the intermediate, between Br_1^0 and Br_2^{-1}, Br state for cell #8 (**Table 2**).

The ~20 eV shoulder in the Br3d spectrum in **Figure 6(b)** conforms well to shake-off transition of the *s*-state in unit cells #8 and #9 with different arrangement of the Br atoms, and there is no solid reason to give preference to a particular cell. The shape and location of the 5–12 eV spectral fragment in **Figure 6(b)**, with due regard to the baseline of this energy region, are consistent with a comparable mixture of CEE transitions calculated for the unit cells #8 and #9. According to DFT data, there is a little difference between cells #6 and #8 (chain type Br) with respect to the shake-off p_y transition, while the cell #6 wins #8 by ~5% in the formation energy. On the contrary, using the cell #7 *hex* instead of #9 Bernal (molecular Br_2) results in larger discordance with the XPS data due to their specific p_x structure. Finally, the unit cell $C_{24}F_{12}Br_2$ #6, with the chain type Br layout, is preferable among others, whereas the energy losses in the Br3d XPS spectrum suggest a mixture ~1:1 of unit cells #6 and #9.

Experimental data have reported the angle α ~30° between the Br-Br axis and C-planes and the molecular Br_2 state for similar to $C_2FBr_{0.15}$ systems [38, 46]. The current combination of XPS and DFT outputs suggests possibility of the chain like bromine arrangement, which can

be realized in appropriate experimental conditions. Besides, the experimental angle (~30°) is close to the weighted average (~29°) of α = 51.5, 17.4, and 18.7° in **Table 2**, which have been found for the most probable unit cells #2, #6, and #9, respectively.

6. Outlook

Any novel approach, including the CEE model, can be truly evaluated by a benefit from its practical application. By an example of the graphite based materials, the chapter has shown how a confluence of the XPS and DFT data can provide additional information on chemical behavior, local geometry and state of the embedded Br_2 molecule and of the other atoms in a sample. A similar treatment can be useful in the field of surface engineering as well, because just a deep knowledge on chemical behavior of a sample can disclose the mechanism and dynamics of its wear performance, thus facilitating the development of advanced materials. The valence band of chemically bound atoms is insensitive to a photoelectron, whose energy it uses for the CEE transition. Then, in the case of the multicomponent materials, agreement or disagreement between energy losses in the XPS spectra of some atoms can be a descriptor of the presence or absence of chemical bonding between these atoms in a sample [17, 19, 22]. Moreover, the state of any component can be traced through change or invariability of the satellites in its XPS spectra, obtained in the course of external influence, thus revealing a wear performance of the material. In case of a "simple" material, the reliable structural data can be used as starting conditions for the appropriate DFT run, which gives comprehensive information on a sample at the atomic level [16, 18]. Extensive use and practice of the XPS and DFT techniques make the CEE analysis easily accessible.

CEE control in a coordinated XPS and DFT study is characterized by the following obvious, verified, and hidden resources.

- Comparison of fine XPS spectra with the calculated CEE transitions can provide the local geometry and bond types in a sample from conventional DFT facilities. The occurrence and consequence of bonding between atoms can be also determined, because the core-level excitation of an atom is accompanied by CEE satellites of the next one only within the integrated valence band.

- The multiple CEE controls (around different XPS peaks) facilitate the data interpretation, while individual sets of the core-level energies improve studying of the multicomponent materials.

- Hydrogen tracing by the XPS, as a specific CEE satellite above the core-level energy of the other sample component, is possible without a contradiction with XPS principles.

- The CEE control is available for samples of any conductivity, because the photoelectron energy losses are linked up to the XPS peak regardless its apparent core-level energy.

- The valence band structure in the XPS spectra differs from that obtained by the nondestructive and theoretical methods. The CEE event is nondestructive as well, because the valence band absorbs only a part of the photoelectron energy for a CEE transition, omitting a destructive force of the incident X-ray impact.

7. Conclusion

Primary collecting of the extra data by a routine technique is always desirable. This chapter highlights a rational model that gives a chance to realize this desire using the conventional XPS and DFT outputs. The model is based on following statements.

- Electronic configuration of the atoms in a solid holds the traps for the energy absorption, such as valence band electron transitions; and the core-level excitation of any origin fills those traps forming the multiple channels for energy dissipation.

- These channels can be traced by the XPS, as the photoelectron energy losses, and by the DFT, as the valence band electron transitions. This pattern does not conflict with general concepts of electron-solid interaction and has been well verified in model studies of Pt and graphite-based materials.

- Intersection of the XPS and DFT outputs carries out two duties. First, it rejects those DFT results which do not conform to the fine XPS spectral structures. Second, it justifies the assignment of the refined DFT data, related to an appropriate unit cell, to a given XPS sample. As a result, the correlated XPS and DFT study discloses hidden potentialities of both techniques and provides the extra data on chemical behavior and local geometry of the atoms in a sample.

- The procedure of a coordinated XPS and DFT study being highlighted can provide a deeper insight into the mechanism of wear performance of the material, thus facilitating the development of advanced composites.

Acknowledgements

Acronyms and abbreviations

AES	auger electron spectroscopy
CEE	conjugate electron excitation
DAPS	disappearance potential spectroscopy
DFT	density functional theory
DOS	density of states
pDOS	partial DOS

1D DOS	one-dimensional DOS
EXAFS	extended X-ray absorption fine structure
HOPG	highly orientated pyrolytic graphite
1 L	1 Langmuir, one second exposure of a gas at pressure of 10^{-6} Torr
ML	1 monolayer coverage of the adsorbate
PAW	projected augmented wave method of the DFT
RAES	resonant auger electron spectroscopy
RIXS	resonant inelastic X-ray scattering
RPES	resonant photoemission electron spectroscopy
Ry	Rydberg, atomic unit of energy close to 13.6 electron volts
XPS	X-ray photoelectron spectroscopy
XAFS	X-ray absorption fine structure
XANES	X-ray absorption near edge structure
UPS	ultraviolet photoelectron spectroscopy
VB	valence band
vdW	van der Waals correction, operating parameter of the DFT

Author details

Alexander R. Cholach

Address all correspondence to: cholach@catalysis.ru

Boreskov Institute of Catalysis, Novosibirsk, Russian Federation

References

[1] Bhanvase BA, Pawade VB, Dhoble SJ, Sh S, Ashokkumar HM, editors. Nanomaterials for Green Energy. 1st ed. Amsterdam: Elsevier; 2018. 500 p. ISBN: 9780128137314

[2] Busca G, editor. Heterogeneous Catalytic Materials. 1st ed. Oxford: Elsevier; 2014. 478 p. ISBN: 9780444595249

[3] Sá J, editor. High Resolution XAS/XES: Analyzing Electronic Structures of Catalysis. Boca Raton: CRC Press; 2014. 214 p. ISBN: 978-1-4665-9298-8

[4] Bunker G. Introduction to XAFS: A Practical Guide to X-ray Absorption Fine Structure Spectroscopy. Cambridge: Cambridge University Press; 2010. 260 p. ISBN: 052176775X

[5] Ament L, van Veenendaal M, Devereau T, Hill J, van den Brink J. Resonant inelastic X-ray scattering studies of elementary excitations. Reviews of Modern Physics. 2011;**83**:705. DOI: 10.1103/RevModPhys.83.705

[6] Brühwiler P, Karis O, Mårtensson N. Charge-transfer dynamics studied using resonant core spectroscopies. Reviews of Modern Physics. 2002;**74**:703. DOI: 10.1103/RevModPhys.74.703

[7] Cholach AR. Advanced power of disappearance potential spectroscopy in the adsorbed species identification. In: Hansen PW, editor. Chemical Physics Research Developments. Hauppauge, New York: Nova Science Publishers; 2011. pp. 149-173. ISBN: 978-1-61122-068-1

[8] Cholach A, Tapilin V. Specific channels for electron energy dissipation in the adsorbed system. The Journal of Chemical Physics. 2013;**138**:104201. DOI: 10.1063/1.4794141

[9] Cholach AR, Tapilin VM. Mechanism of conjugate electron transitions on the surface of a solid. Journal of Structural Chemistry. 2015;**56**:589-595. DOI: 10.1134/S0022476615030282

[10] Cholach AR, Tapilin VM. The bulk of evidence for novel electron transitions above the core level threshold. Russian Journal of Physical Chemistry A. 2015;**89**:2402-2406. DOI: 10.1134/S0036024415130105

[11] Cholach A, Tapilin V. Adsorption of small molecules on the Pt(100) single crystal surface studied by disappearance potential spectroscopy. Applied Surface Science. 2001;**180**: 173-183. DOI: 10.1016/S0169-4332(01)00332-4

[12] Briggs D, Seach M, editors. Practical Surface Analysis by Auger and X-ray Photoelectron Spectroscopy. Chichester: Wiley; 1983. 674 p. ISBN: 9780471953401

[13] Woodruff D, Delchar T, editors. Modern Techniques of Surface Science. 2nd ed. Cambridge: Cambridge University Press; 1994. 608 p. ISBN: 9780521424981

[14] Rabalais J. Principles of Ultraviolet Photoelectron Spectroscopy. NY: Wiley; 1977. 472 p. ISBN: 0471702854

[15] Chouhan A, Mungse HP, Sharma OP, Singh RK, Khatri OP. Chemically functionalized graphene for lubricant applications: Microscopic and spectroscopic studies of contact interfaces to probe the role of graphene for enhanced tribo-performance. Journal of Colloid and Interface Science. 2018;**513**:666-676. DOI: 10.1016/j.jcis.2017.11.072

[16] Rodrigues SP, Evaristo M, Carvalho S, Cavaleiro A. Fluorine-carbon doping of WS-based coatings deposited by reactive magnetron sputtering for low friction purposes. Applied Surface Science. 2018;**445**:575-585. DOI: 10.1016/j.apsusc.2018.03.113

[17] Ju H, Yu D, Yu L, Ding N, Xu J, Zhang X, Zheng Y, Yang L, He X. The influence of Ag contents on the microstructure, mechanical and tribological properties of ZrN-Ag films. Vacuum. 2018;**148**:54-61. DOI: 10.1016/j.vacuum.2017.10.029

[18] Long J, Zhang W, Wang Y, Du Y, Zhang Z, Lu B, Cheng K, Peng Y. A new type of WC-Co-Ni-Al cemented carbide: Grain size and morphology of γ'-strengthened composite binder phase. Scripta Materialia. 2017;**126**:33-36. DOI: 10.1016/j.scriptamat.2016.08.007

[19] Fernandes F, Danek M, Polcar T, Cavaleiro A. Tribological and cutting performance of TiAlCrN films with different Cr contents deposited with multilayered structure. Tribology International. 2018;**119**:345-353. DOI: 10.1016/j.triboint.2017.11.008

[20] Marchetto D, Restuccia P, Ballestrazzi A, Righi MC, Rota A, Valeri S. Surface passivation by graphene in the lubrication of iron: A comparison with bronze. Carbon. 2017;**116**: 375-380. DOI: 10.1016/j.carbon.2017.02.011

[21] Oh D-S, Kang K-H, Kim H-J, Kim J-K, Won M-S, Kim D-E. Tribological characteristics of micro-ball bearing with V-shaped grooves coated with ultra-thin protective layers. Tribology International. 2018;**119**:481-490. DOI: 10.1016/j.triboint.2017.11.014

[22] Wen X, Liang K, Tian L, Shi K, Zheng J. Al_2O_3 coating on $Li_{1.256}Ni_{0.198}Co_{0.082}Mn_{0.689}O_{2.25}$ with spinel-structure interface layer for superior performance lithium ion batteries. Electrochimica Acta. 2018;**260**:549-556. DOI: 10.1016/j.electacta.2017.12.120

[23] Liu LC, Corma A. Metal catalysts for heterogeneous catalysis: From single atoms to nanoclusters and nanoparticles. Chemical Reviews. 2018;**118**:4981-5079. DOI: 10.1021/acs.chemrev.7b00776

[24] Sedelnikova O, Bulusheva L, Asanov I, Yushina I, Okotrub A. Energy shift of collective electron excitations in highly corrugated graphitic nanostructures: Experimental and theoretical investigation. Applied Physics Letters. 2014;**104**:161905. DOI: 10.1063/1.4873123

[25] Tsuei K-D, Yuh J-Y, Tzeng C-T, Chu R-Y, Chung S-C, Tsang K-L. Photoemission and photoabsorption study of C_{60} adsorption on Cu(111) surfaces. Physical Review B. 1997; **56**:15412. DOI: 10.1103/PhysRevB.56.15412

[26] Shulga YM, Tien T-C, Huang C-C, Lo SC, Muradyan VE, Polyakova NV, Ling Y-C, Loutfy RO, Moravsky AP. XPS study of fluorinated carbon multi-walled nanotubes. Journal of Electron Spectroscopy and Related Phenomena. 2007;**160**:22-28. DOI: 10.1016/j.elspec.2007.06.002

[27] Bourlinos AB, Safarova K, Siskova K, Zbořil R. The production of chemically converted graphenes from graphite fluoride. Carbon. 2012;**50**:1425-1428. DOI: 10.1016/j.carbon.2011.10.012

[28] Nakajima T. Surface Mmodification of carbon anodes for lithium ion batteries by fluorine and chlorine. In: Nakajima T, Groult H, editors. Advanced Fluoride-Based Materials for Energy Conversion. Amsterdam: Elsevier; 2015. pp. 203-223. ISBN: 978-0-12-800679-5

[29] Asanov IP, Okotrub AV, Gusel'nikov AV, Yushina IV, Vyalikh DV, Bulusheva LG. Charge-induced formation of thin conducting layers on fluorinated graphite surface. Carbon. 2015;**82**:446-458. DOI: 10.1016/j.carbon.2014.10.088

[30] Cholach AR, Asanov IP, Bryliakova AA, Okotrub AV. Extra electronic outer-shell peculiarities accessible under a joint XPS and DFT study. Physical Chemistry Chemical Physics. 2017;**19**:15842-15848. DOI: 10.1039/c7cp00900c

[31] Cholach AR, Asanov IP, Bryliakova AA. Identification of conjugate electron transitions in X-ray photoelectron spectra. Journal of Structural Chemistry. 2017;**58**:1160-1165. DOI: 10.1134/S0022476617060130

[32] Kirschner J. Electron-excited core level spectroscopies. In: Ibach H, editor. Electron Spectroscopy for Surface Analysis. Berlin: Springer; 1977. pp. 59-115. ISBN: 978-3-642-81099-2

[33] Brodén G, Pirug G, Bonzel H. Chemisorption of CO on the unreconstructed Pt(100) surface. Surface Science. 1978;**72**:45-52. DOI: 10.1016/0039-6028(78)90376-X

[34] Lide D, editor. CRC Handbook of Chemistry and Physics. 85th ed. Boca Raton: CRC Press; 2005. 2616 p. ISBN: 9780849304859

[35] Tougaard S, Chorkendorff I. Differential inelastic electron scattering cross sections from experimental reflection electron-energy-loss spectra: Application to background removal in electron spectroscopy. Physical Review B. 1987;**35**:6570. DOI: 10.1103/PhysRevB.35.6570

[36] Shubin YV, Pinakov DV, Chekhova GN, Alferova NI, Logvinenko VA. Phase transitions of intercalation inclusion compounds $C_2F_{0.92}Br_{0.0}\cdot yCH_3CN$ in the temperature range 20-260°C. Journal of Structural Chemistry. 2006;**47**:1141-1154. DOI: 10.1007/s10947-006-0437-y

[37] Asanov I, Bulusheva L, Dubois M, Yudanov N, Alexeev A, Makarova T, Okotrub AV. Graphene nanochains and nanoislands in the layers of room-temperature fluorinated graphite. Carbon. 2013;**59**:518-529. DOI: 10.1016/j.carbon.2013.03.048

[38] Bausk N, Erenburg S, Yudanov N, Mazalov L. Geometry and orientation of molecules in a graphite fluoride matrix. Journal of Structural Chemistry. 1996;**37**:913-919. DOI: 10.1007/BF02439075

[39] Giannozzi P, Baroni S, Bonini N, Calandra M, Car R, Cavazzoni C, Ceresoli D, Chiarotti GL, Cococcioni M, Dabo I, Dal Corso A, de Gironcoli S, Fabris S, Fratesi G, Gebauer R, Gerstmann U, Gougoussis C, Kokalj A, Lazzeri M, Martin-Samos L, Marzari N, Mauri F, Mazzarello R, Paolini S, Pasquarello A, Paulatto L, Sbraccia C, Scandolo S, Sclauzero G, Seitsonen AP, Smogunov A, Umari P, Wentzcovitch RM. QUANTUM ESPRESSO: A modular and open-source software project for quantum simulations of materials. Journal of Physics: Condensed Matter. 2009;**21**:395502. DOI: 10.1088/0953-8984/21/39/395502

[40] Perdew J, Ruzsinszky A, Csonka G, Vydrov O, Scuseria G, Constantin L, Zhou X, Burke K. Restoring the density-gradient expansion for exchange in solids and surfaces. Physical Review Letters. 2008;**100**:136406. DOI: 10.1103/PhysRevLett.100.136406

[41] Blöchl P. Projector augmented-wave method. Physical Review B. 1994;**50**:17953. DOI: 10.1103/PhysRevB.50.17953

[42] Marzari N, Vanderbilt D, De Vita A, Payne M. Thermal contraction and disordering of the Al(110) surface. Physical Review Letters. 1999;**82**:3296. DOI: 10.1103/PhysRevLett.82.3296

[43] Grimme S. Semiempirical GGA-type density functional constructed with a long-range dispersion correction. Journal of Computational Chemistry. 2006;**27**:1787-1799. DOI: 10.1002/jcc.20495

[44] Perdew J, Burke K, Ernzerhof M. Generalized gradient approximation made simple. Physical Review Letters. 1996;**77**:3865. DOI: 10.1103/PhysRevLett.77.3865

[45] Hu C-H, Zhang P, Liu H-Y, Wu S-Q, Yang Y, Zhu Z-Z. Structural stability and electronic and magnetic properties of fluorinated bilayer graphene. The Journal of Physical Chemistry C. 2013;**117**:3572-3579. DOI: 10.1021/jp3103113

[46] Feldman J, Elam W, Ehrlich A, Skelton E, Dominguez D, Chung D, Lytle F. Polarized-X-ray-absorption studies of graphite intercalated-bromine compounds. Physical Review B. 1986;**33**:7961. DOI: 10.1103/PhysRevB.33.7961

[47] Monkhorst H, Pack J. Special points for Brillouin-zone integrations. Physical Review B. 1976;**13**:5188. DOI: 10.1103/PhysRevB.13.5188

[48] Rother A, Scheerschmidt K. Relativistic effects in elastic scattering of electrons in TEM. Ultramicroscopy. 2009;**109**:154-160. DOI: 10.1016/j.ultramic.2008.08.008

[49] Gingrich DM, editor. Practical Quantum Electrodynamics. NY: CRC Press; 2006. 360 p. ISBN: 9781584885429

[50] Kittel C, editor. Introduction to Solid State Physics. 8th ed. NY: Wiley; 2004. 704 p. ISBN: 9780471415268

[51] Pennemann B, Oster K, Wandelt K. Hydrogen adsorption on Pt(100) at low temperatures: Work function and thermal desorption data. Surface Science. 1991;**249**:35-43. DOI: 10.1016/0039-6028(91)90831-C

[52] Bonzel H, Fischer T. An UV photoemission study of NO and CO adsorption on Pt (100) and Ru (10-10) surfaces. Surface Science. 1975;**51**:213-227. DOI: 10.1016/0039-6028(75)90244-7

[53] Ramstad A, Strisland F, Raaen S, Borg A, Berg C. CO and O_2 adsorption on the Re/Pt(111) surface studied by photoemission and thermal desorption. Surface Science. 1999; **440**:290-300. DOI: 10.1016/S0039-6028(99)00827-4

[54] Bartram M, Koel B, Carter E. Electronic effects of surface oxygen on the bonding of NO to Pt(111). Surface Science. 1989;**219**:467-489. DOI: 10.1016/0039-6028(89)90522-0

[55] Demuth J. Ultraviolet photoemission studies of hydrogen chemisorption bonding to Ni, Pd and Pt surfaces. Surface Science. 1977;**65**:369-375. DOI: 10.1016/0039-6028(77)90317-X

[56] den Boer M, Einstein T, Elam W, Park R, Roelofs L, Laramore G. Extended appearance-potential fine-structure analysis: oxygen on Al(100). Physical Review Letters. 1980;**44**:496. DOI: 10.1103/PhysRevLett.44.496

[57] Puglia C, Nilsson A, Hernnäs B, Karis O, Bennich P, Mårtensson N. Physisorbed, chemisorbed and dissociated O_2 on Pt(111) studied by different core level spectroscopy methods. Surface Science. 1995;**342**:119-133. DOI: 10.1016/0039-6028(95)00798-9

[58] Sakai Y, Saito S, Cohen ML. Lattice matching and electronic structure of finite-layer graphene/h-BN thin films. Physical Review B. 2014;**89**:115424. DOI: 10.1103/PhysRevB.89.115424

[59] Taft E, Phillipp H. Optical properties of graphite. Physical Review. 1965;**138**:A197. DOI: 10.1103/PhysRev.138.A197

[60] Sedelnikova O, Bulusheva L, Okotrub A. Modulation of electronic density in waved graphite layers. Synthetic Metals. 2010;**160**:1848-1855. DOI: 10.1016/j.synthmet.2010.07.001

[61] Rolere S, Goulon J-F, Poncin-Epaillard F. Influence of the curing temperature on the diffusion rate of the perfluorinated alkyl chains of a modified epoxy resin. European Polymer Journal. 2017;**91**:61-69. DOI: 10.1016/j.eurpolymj.2017.03.053

[62] Bulusheva L, Tur V, Fedorovskaya E, Asanov I, Pontiroli D, Riccò M, Okotrub A. Structure and supercapacitor performance of graphene materials obtained from brominated and fluorinated graphites. Carbon. 2014;**78**:137-146. DOI: 10.1016/j.carbon.2014.06.061

[63] Powell BM, Heal KM, Torrie BH. The temperature dependence of the crystal structures of the solid halogens, bromine and chlorine. Molecular Physics. 1984;**53**:929-939. DOI: 10.1080/00268978400102741